

# SUBSAMPLING, ALIGNING, AND AVERAGING TO FIND CIRCULAR COORDINATES IN RECURRENT TIME SERIES

ANDREW J. BLUMBERG, MATHIEU CARRIÈRE, JUN HOU FUNG,  
AND MICHAEL A. MANDELL

**ABSTRACT.** We introduce a new algorithm for finding robust circular coordinates on data that is expected to exhibit recurrence, such as that which appears in neuronal recordings of *Caenorhabditis elegans*. Techniques exist to create circular coordinates on a simplicial complex from a dimension 1 cohomology class, and these can be applied to the Rips complex of a dataset when it has a prominent class in its dimension 1 cohomology. However, it is known this approach is extremely sensitive to uneven sampling density.

Our algorithm comes with a new method to correct for uneven sampling density, adapting our prior work on averaging coordinates in manifold learning. We use rejection sampling to correct for inhomogeneous sampling and then apply Procrustes matching to align and average the subsamples. In addition to providing a more robust coordinate than other approaches, this subsampling and averaging approach has better efficiency.

We validate our technique on both synthetic data sets and neuronal activity recordings. Our results reveal a topological model of neuronal trajectories for *C. elegans* that is constructed from loops in which different regions of the brain state space can be mapped to specific and interpretable macroscopic behaviors in the worm.

## CONTENTS

1. Introduction	1
2. Finding circular coordinates using persistent cohomology	3
3. Density uniformization via rejection sampling	4
4. Averaging coordinates with Procrustes alignment and hill climbing	7
5. Experimental results	11
6. Discussion	20
References	21

## 1. INTRODUCTION

In this paper, we consider coordinates on recurrent time series data. Good coordinates should reflect this recurrence and so should take values on a circle. There has been a substantial literature on producing coordinates of this type (e.g., [25, 9, 47] in the context of neuronal activity). The work of de Silva, Morozov, and

---

The first author was partially supported by the NSF grant DMS-1912194 and by ONR grant N00014-22-1-2679.

The third author was supported by the NSF grant DMS-1912194.

The fourth author was supported by the ONR grant N00014-22-1-2675.

Vejdemo-Johansson [42] introduced the idea of using techniques from *topological data analysis* (TDA) to find circular coordinates, specifically *persistent cohomology*. Their basic approach is to infer a cohomology class and choose a specific cocycle representative that is the smoothest, which amounts to solving a least-squares optimization problem. In [45], these techniques were applied to detect and quantify recurrent patterns in human motions.

TDA methods have qualitative differences from competing approaches that make them particularly attractive for exploratory data analysis. For example, when the feature scale is unknown, persistent cohomology can be used to find a range of scales where the coordinate appears the most robust. However, as a consequence of the optimization scheme used to produce a cohomology class representative, regions that are more densely sampled tend to be represented by smaller changes in the coordinate. This issue was identified in [39] where a renormalization technique was introduced to try to correct for uneven sampling. Similarly, [33] proposed using weighted Laplacians or  $L^p$ -optimization to infer robust circular coordinates. Another issue that arises is that the computational cost of computing the persistent cocycle is prohibitive even for moderately large data sets. This was addressed in [36] by aggressively choosing landmarks and using those to compute coordinates. There, an adapted version of the weighting scheme of [39] was used to handle uneven density and possible sensitivity to the specific choice of landmarks. On the other hand, the use of landmarks is particularly sensitive to errors introduced by noise and outliers.

We introduce a new algorithm for finding circular coordinates that does not require an ad hoc weighting scheme, is insensitive to uneven sampling density, and is robust to noise and outliers, while retaining efficiency. At a high level, our algorithm is comprised of the following steps:

- (1) *Rejection sampling.* We apply density-based rejection sampling to the data to produce a number of subsample data sets that with high probability correct for uneven sampling of the original data.
- (2) *Persistent cohomology.* We identify a long bar in the first persistent cohomology group  $PH^1$  on each subsample, which we use to obtain a circular coordinate adapted to that subsample.
- (3) *Alignment and averaging.* We align and average the resulting coordinates to obtain a final coordinate on the entire data set.

We use standard density estimation techniques to carry out the rejection sampling; these can be shown to be asymptotically correct and work well in practice. For the alignment and averaging, we build on our prior work [7] that uses the solution to the generalized Procrustes problem to align and average different Euclidean coordinates. We use  $O(2)$  Procrustes alignment on  $\mathbb{R}^2$  to produce an initial seed for a hill climbing algorithm to search for the best alignment of circular coordinates for averaging.

We applied our rejection sampling, alignment, and averaging algorithm to extract circular coordinates from whole-brain neuronal recordings from the nematode *C. elegans*. There is a recurrent locomotory cycle reflected in the worm's neuronal activity, which explains why circular coordinates are sensible. We found coordinates for a variety of worm neuronal trajectories, providing a basis for further scientific analysis of stimulus response. Furthermore, we validated our approach using an information-theoretic criterion, showing that the resulting coordinates are

more informative than the uncorrected coordinates. Finally, we observed significant time savings from computing and aggregating persistent cocycle representatives on subsamples.

**Outline.** Section 2 reviews the use of persistent cohomology to find circular coordinates. Section 3 describes the method for performing rejection sampling to construct the subsamples for circular coordinates. Section 4 describes the algorithm to take the coordinates on the subsamples and build a coordinate on the whole data set by alignment and averaging. Section 5 presents experimental results of our algorithm applied to synthetic and real world data.

**Acknowledgments.** We thank Raúl Rabadán and Eviatar Yemini for many helpful conversations related to the subject of this paper.

## 2. FINDING CIRCULAR COORDINATES USING PERSISTENT COHOMOLOGY

In this section, we review techniques from *topological data analysis* (TDA) for extracting circular coordinates from high-dimensional data, following work of [42], [39], and [36].

The basic overall process of generating *circular coordinates*  $X \rightarrow S^1$  from a data set  $X$  is as follows:

- (1) We construct a filtered simplicial complex  $K_\bullet$ , the Vietoris-Rips complex, on the data set  $X$ . The filtration encodes information about the shape of the data as a scale parameter  $\epsilon$  varies.
- (2) We compute the first persistent cohomology  $PH^1$  of this filtered complex, and find a cohomology class which is present across a wide range of feature scales (the “longest bar”).
- (3) We identify the value of the scale parameter  $\epsilon$  within the longest bar, following [39].
- (4) We perform an optimization process to extract a coordinate map  $\bar{f}$  to  $S^1$  from this persistent cohomology class.

We assume the reader is familiar enough with TDA that the first two steps do not require additional exposition. (See for example [11, 20, 24] for a basic overview or [16, 32, 13, 37] for more detailed treatments.) We also point out that the theoretical aspects of ensemble approaches to persistent homology, similar to what we shall describe later, have been recently explored [43].

In step 3, it may be the case that the scale parameter is not very large. There are many possible heuristics for what “large” means; for example, comparison to ensure the scale parameter is substantially larger than the median  $k$ th nearest neighbor length for  $k = 3$  is a common criterion. In such a case, it is reasonable to infer that cohomology classes in  $PH^1$  are either too small to reflect actual geometry in the data or the geometry underlying the point cloud cannot be adequately described by a circular coordinate. This ability to detect cases when the assumed geometric model is misspecified is a strength of the TDA approach. We can optionally alert the user when the identified bar is too small. Moreover, if there are multiple large bars, we can notify the user that there may be multiple independent and informative coordinates.

We now give a terse review of the procedure in step 4, based on [42]. A foundational result in algebraic topology is that for a simplicial complex  $K_\bullet$ , elements of  $H^1(K_\bullet; \mathbb{Z})$  are in one-to-one correspondence with homotopy classes of maps from

the geometric realization  $K$  to  $S^1$ . There is a straightforward way to go from an integral 1-cocycle  $\alpha$  to such a map: having chosen a well-ordering of the vertices of  $K_\bullet$ , the data in  $\alpha$  (the cochain itself) is an integer-valued function on the set of edges. The map that sends all vertices of  $K_\bullet$  to a given basepoint of  $S^1$  and sends each edge  $e$  to  $S^1$  by wrapping around  $\alpha(e)$  times (using the orientation from the ordering of vertices) gives a map  $K \rightarrow S^1$  in the corresponding homotopy class. In our setting, this construction is useless because when  $K_\bullet$  is the Vietoris-Rips complex of a data set, the resulting coordinate map  $\bar{f}$  on the data set is a constant map.

To address this issue, de Silva, Morozov, and Vejdemo-Johansson [42] propose a method using real cocycles. In the following,  $C^n(K_\bullet, A)$  denotes cochains with coefficients in  $A$  (functions from  $K_n$  to  $A$ ), and  $\delta$  represents the differential in the cochain complex.

**Proposition 2.1** ([42, Proposition 2]). *Let  $[\tilde{\alpha}] \in \text{im}(H^1(K_\bullet; \mathbb{Z}) \rightarrow H^1(K_\bullet; \mathbb{R}))$  and let  $\tilde{\alpha}$  be a cocycle representative of the form  $\tilde{\alpha} = \alpha + \delta f$  for some  $\alpha \in C^1(K_\bullet; \mathbb{Z})$  and  $f \in C^0(K_\bullet; \mathbb{R})$ . Then there is a continuous function  $K \rightarrow \mathbb{R}/\mathbb{Z}$  that sends each  $x \in K_0$  to  $f(x) \pmod{\mathbb{Z}}$  and each  $e \in K_1$  to an interval of (signed) length  $\tilde{\alpha}(e)$ .*

In the case when  $K_\bullet$  is the Vietoris-Rips complex of a data set  $X$  at a scale  $\epsilon$ , the set of vertices  $K_0$  is  $X$  and we get coordinates  $X \rightarrow \mathbb{R}/\mathbb{Z}$  given by the function in the proposition. Namely,  $x \in X$  goes to the reduction mod  $\mathbb{Z}$  of  $f(x)$ . To get circular coordinates  $X \rightarrow S^1$  with  $S^1$  modeled as  $\mathbb{R}/2\pi\mathbb{Z}$ , we take  $\bar{f}(x) = 2\pi f(x)$ . For  $S^1$ , modeled as the unit circle in  $\mathbb{R}^2$ , we take  $\bar{f}(x) = (\cos(2\pi f(x)), \sin(2\pi f(x)))$ .

The procedure is then to start with an integral 1-cocycle  $\alpha$  and produce an appropriate real cocycle  $\tilde{\alpha}$  that is cohomologous to  $\alpha$  in  $C^1(K_\bullet; \mathbb{R})$ . The approach of [42] suggests using the “harmonic” representative, that is, the one that minimizes the energy functional

$$E(\tilde{\alpha}) = \sum_{e \in K_1} \tilde{\alpha}(e)^2.$$

Since we are solving the problem over the space  $\tilde{\alpha} = \alpha + \delta f$ , if we rewrite in terms of  $f$  we can implement this by solving a least squares problem in the variables given by  $K_0$ . This has a unique solution provided every vertex lies on some edge. Otherwise, isolated vertices give free parameters in the solution, and this amounts to assigning them arbitrary circular coordinates.

### 3. DENSITY UNIFORMIZATION VIA REJECTION SAMPLING

The process described in the previous section is sensitive to the density variation within the point cloud. Non-uniform sampling causes distortion in the circular coordinates, as we illustrate in subsection 5.1. This section explains a general procedure to fix this problem using rejection sampling.

The problem of non-uniform sampling distorting circular coordinates is well-known and has been studied before. For example, Rybakken, Baas, and Dunn [39], Perea [36], and Paik and Park [33] propose additional steps to help ameliorate density imbalances when computing circular coordinates. These works suggest modifying the optimization problem to find a “weighted” harmonic representative, where the weights come from an altered metric on the underlying space that accounts for density. There are different possible heuristics for choosing these weights.

Rather than attempting to infer weights based on density variations, we directly equalize the density by rejection sampling and average the resulting coordinates using Procrustes alignment of the coordinates produced from subsamples. This procedure has several notable advantages. First, averaging produces more robust coordinates that are less sensitive to outliers (e.g., see [7] for a discussion of this in the context of manifold learning). Second, it is simple and easy to generalize. Third, we can use existing theoretical work on density estimation to justify the subsampling procedure, whereas there does not seem to be complete justification for any of the existing weighting heuristics.

We begin by reviewing rejection sampling in the geometric context. Let  $M$  be a  $d$ -dimensional compact submanifold of  $\mathbb{R}^N$ , with inherited Riemannian metric  $d_M$  and volume form  $\mu$ . We assume that we only have access to samples of  $M$  from a different unknown density  $\rho$ . Let  $X$  be a sample of points in  $M$  drawn with density  $\rho$ . Given a function  $\pi: M \rightarrow [0, 1]$ , *rejection sampling* weighted by  $\pi$  forms a subsample  $Y$  from  $X$  where for each point  $x \in X$ , we accept  $x$  into  $Y$  with probability  $\pi(x)$ . If we choose  $\pi(x)$  proportional to  $1/\rho(x)$ , then  $Y$  becomes distributed according to  $\mu$ : by Bayes' theorem, for a Borel measurable subset  $U \subseteq M$ , for each point  $y$  in  $Y$ , the probability that  $y$  belongs to  $U$  is

$$\frac{\int_U \pi(x)\rho(x) d\mu(x)}{\int_M \pi(x)\rho(x) d\mu(x)} = \frac{\mu(U)}{\mu(M)}.$$

Of course, the density  $\rho$  is not known a priori, so we have to estimate it. The problem of density estimation is classical and well-studied. For instance, density estimators based on constructing an empirical density function go back to Fix and Hodges [18], Rosenblatt [38], and Parzen [34]. Estimators based on nearest neighbor distances were originally proposed by Loftsgaarden and Quesenberry [26]. For textbook references on density estimation, see [15, 41]. Recently, there has been renewed interest in these types of density estimates and their extensions in the context of geometric inference; see [6, 12]. Moreover, density estimation on unknown submanifolds has also been specifically explored in [3, 21]. We do not claim particular originality for our discussion below; the result we prove is very similar to existing results, slightly generalized to fit our specific setup.

For simplicity, we work with a density estimator of the following form. Fix  $\epsilon > 0$ . Let

$$(3.1) \quad \hat{\rho}_\epsilon(x) = \frac{1}{V_d \epsilon^d} \frac{\#(X \cap B_\epsilon(x))}{\#X},$$

where  $B_\epsilon(x)$  is a ball of radius  $\epsilon$  centered at  $x$  in  $\mathbb{R}^N$  and  $V_d$  is the volume of the  $d$ -dimensional unit ball. A different approach is to use density estimators based on codensity or kernel methods; we found in practice that the basic density estimator above was effective enough.

To establish the consistency of this estimator, we begin with an elementary geometric lemma estimating the measure of a ball on the manifold. Recall that the *reach* of a smooth compact submanifold  $M$  in  $\mathbb{R}^N$  is the supremum of the real numbers  $r$  such that every point in the  $r$ -neighborhood of  $M$  has a unique closest point to  $M$ .

**Lemma 3.2.** *Let  $\epsilon$  be smaller than the reach of  $M$ . Then for  $x \in M$ ,*

$$\frac{\mu(M \cap B_\epsilon(x))}{V_d \epsilon^d} = 1 + O(\epsilon).$$

*Proof.* We estimate the volume  $\mu(M \cap B_\epsilon(x))$  as follows. First, observe that there exists  $\epsilon' = \epsilon + O(\epsilon^2)$  such that

$$\mu(B_\epsilon^M(x)) \leq \mu(M \cap B_\epsilon(x)) \leq \mu(B_{\epsilon'}^M(x)).$$

The first inequality is immediate and the second follows from the fact that if the Euclidean distance from  $y \in M$  to  $x$  is less than twice the reach, then

$$d_M(x, y) \leq d_{\mathbb{R}^n}(x, y) + O(d_{\mathbb{R}^n}(x, y)^2).$$

(One can give a direct proof by estimating arclength and using the exponential map; see e.g., [8, Lemma 3], [2, Lemma 4.3], or [5, Lemma 3]). Therefore,  $M \cap B_\epsilon(x) \subseteq B_{\epsilon'}^M(x)$  for  $\epsilon'$  large enough and on the order of  $\epsilon + O(\epsilon^2)$ , which implies the inequality.

Next, we can estimate  $\mu(B_\epsilon^M(x))$  in terms of  $\mu(B_\epsilon^{\mathbb{R}^d}) = V_d \epsilon^d$  and higher corrections coming from the scalar curvature  $S$ :

$$\mu(B_\epsilon^M(x)) = V_d \epsilon^d \left( 1 - \frac{S(x)}{6(d+2)} \epsilon^2 + O(\epsilon^4) \right).$$

As a consequence, we have that

$$\mu(B_\epsilon^M(x)) = V_d \epsilon^d (1 + O(\epsilon)).$$

Putting this all together, we conclude that

$$\mu(M \cap B_\epsilon(x)) = V_d \epsilon^d (1 + O(\epsilon)). \quad \square$$

Applying the lemma, we can now prove the consistency of the density estimator.

**Proposition 3.3.** *Suppose  $M$  is a compact  $d$ -dimensional smooth submanifold of  $\mathbb{R}^n$  with inherited volume form  $\mu$ . Let  $\rho$  be a density supported on all of  $M$ . Let  $X$  be a collection of iid samples drawn from  $\rho$ , and  $\epsilon$  a bandwidth parameter. Then for all  $x \in M$  that are points of continuity for  $\rho$ , the quantity  $\hat{\rho}_\epsilon(x)$  converges in probability to  $\rho(x)$  as  $\#X \rightarrow \infty$ , provided  $\epsilon \rightarrow 0$  and  $\epsilon(\#X)^{1/2d} \rightarrow \infty$ .*

*Proof.* The idea is that the law of large numbers implies

$$\lim_{\#X \rightarrow \infty} \frac{\#(X \cap B_\epsilon(x))}{\#X} = \int_{M \cap B_\epsilon(x)} \rho d\mu.$$

Let us make this more precise. First, using the preceding lemma and the continuity of  $\rho$  we have

$$\frac{1}{V_d \epsilon^d} \int_{M \cap B_\epsilon(x)} \rho d\mu = \frac{1 + O(\epsilon)}{\mu(M \cap B_\epsilon(x))} \int_{M \cap B_\epsilon(x)} \rho d\mu \xrightarrow{\epsilon \rightarrow 0} \rho(x).$$

Hence for  $t > 0$ , we have

$$\begin{aligned} & \mathbb{P}(|\hat{\rho}_\epsilon(x) - \rho(x)| \geq t) \\ & \leq \mathbb{P} \left( \left| \hat{\rho}_\epsilon(x) - \frac{1}{V_d \epsilon^d} \int_{M \cap B_\epsilon(x)} \rho d\mu \right| \geq t + O(\epsilon) \right) \\ & = \mathbb{P} \left( \left| \frac{\#(X \cap B_\epsilon(x))}{\#X} - \int_{M \cap B_\epsilon(x)} \rho d\mu \right| \geq V_d \epsilon^d (t + O(\epsilon)) \right) \\ & \leq 2 \exp(-2(\#X)(V_d \epsilon^d (t + O(\epsilon)))^2) \end{aligned}$$

where the last line uses Hoeffding's inequality.

Consequently, if  $\epsilon(\#X)^{1/2d} \rightarrow \infty$ , then  $\hat{\rho}_\epsilon(x)$  converges to  $\rho(x)$  in probability as  $\#X \rightarrow \infty$  and  $\epsilon \rightarrow 0$ .  $\square$

*Remark 3.4.* To get a *point* estimate of density, we need  $\epsilon$  to tend to zero, but the formula in the proposition indicates that it cannot go to zero too quickly, and the rate at which it can go to 0 is controlled by the dimension  $d$ . A larger  $d$  forces a slower approach to zero; this is an example of the so-called *curse of dimensionality*.

*Remark 3.5.* Recall that we only need an estimator that is proportional to density. Therefore, we might as well use

$$(3.6) \quad \hat{\rho}_\epsilon(x) = \#(X \cap B_\epsilon(x))$$

instead, i.e., simply count the number of points in an  $\epsilon$ -neighborhood of  $x \in \mathbb{R}^n$  without dividing by the total number of points and the volume of a standard ball. In particular, while the consistency of the estimator may depend on the intrinsic dimension  $d$  of the underlying manifold, the estimator itself does not, up to global scaling.

*Remark 3.7.* We offer a heuristic for choosing the bandwidth parameter  $\epsilon$  for the density estimator. According to the multivariate *Scott's rule* [41], we can set

$$\epsilon = \hat{\sigma} \cdot (\#X)^{-1/(d+4)},$$

where  $\hat{\sigma}^2 = \det(\hat{\Sigma})^{1/d}$  is the geometric mean of the eigenvalues of the positive-definite sample covariance matrix  $\hat{\Sigma}$  of  $X$ .

For this rule to satisfy the conditions of Proposition 3.3, we would need

$$(\#X)^{1/(d+4)-1/(2d)} \ll \hat{\sigma} \ll (\#X)^{1/(d+4)}$$

asymptotically. In particular, if  $d$  is not sufficiently small, then surprisingly  $\hat{\sigma}$  has to *grow* with  $\#X$ . Hence, this heuristic is perhaps best used when the intrinsic dimension  $d$  is small.

Alternatively, the value of the hyperparameter  $\epsilon$  can be manually tuned, for example by maximizing the mutual information metric we describe in Section 5.3.

The above discussion provides the theoretical justification for the following standard rejection sampling procedure to generate an ensemble of subsamples on which to produce circular coordinates.

**Input:** A data set  $X \subset \mathbb{R}^N$ .

**Step 1:** For each point  $x \in X$ , compute  $\hat{\rho}_\epsilon(x)$  by the formula (3.6). We define  $\pi: X \rightarrow [0, 1]$  to be  $x \mapsto m/\hat{\rho}_\epsilon(x)$  where  $m \leq \min_x \hat{\rho}_\epsilon(x)$  is chosen to guarantee a given expected subsample size.

**Step 2:** For  $i = 1, \dots, k$ , create  $X_i$  as follows. For each point  $z \in X$ , draw a uniform random number  $\tau_{i,z} \in [0, 1]$  and accept  $z$  in  $X_i$  if and only if  $\tau_{i,z} \leq \pi(x)$ .

**Step 3:** Return subsamples  $X_1, \dots, X_k$ .

#### 4. AVERAGING COORDINATES WITH PROCRUSTES ALIGNMENT AND HILL CLIMBING

The purpose of this section is to explain an algorithm for averaging circular coordinates produced on subsamples of data. We do this by adapting the “align and average” framework for manifold learning from our previous paper [7]. The basic outline is that we use the Procrustes problem to align the data sets and then take a suitable mean. We begin by reviewing the Procrustes problem specialized to the circle.

**Definition 4.1.** The *generalized Procrustes problem on the circle* is the following: given a set of  $k$  input configurations of  $n$  ordered points on  $S^1$ , each represented as a function  $\Phi_i : \{1, \dots, n\} \rightarrow S^1$ , determine the optimal rotations and reflections  $g_1, \dots, g_k$  and centroid configuration  $\Theta$  that minimizes the loss functional

$$L((g_1, \dots, g_k), \Theta) = \frac{1}{k} \sum_{i=1}^k \sum_{j=1}^n d_{S^1}(g_i \cdot \Phi_i(j), \Theta(j))^2.$$

Algorithms to find approximate solutions to the corresponding problem in Euclidean space go back more than 50 years, and in [7] the authors used such algorithms to average dimensionality-reducing embeddings on subsamples. In contrast to the current paper, [7] did not perform density equalization and assumed large overlap between subsamples; the Procrustes solution algorithms extend to this “missing values” case. In this paper, subsamples are not expected to have large overlap, and Procrustes solution algorithms do not readily adapt to this context: when data sets do not overlap, it does not make sense to ask for an alignment. Therefore, the problem and approach in this paper differ from [7] in two fundamental ways: first, we study circular coordinates instead of embeddings into Euclidean space, and second, instead of approximating the solution to the missing values Procrustes problem on the subsample coordinates, we first extend the subsample coordinates to the whole data set and then find the approximate solution to the Procrustes problem on the circle (Definition 4.1).

Assume we are given subsamples  $X_i \subset X$ ,  $i = 1, \dots, k$  each with coordinates  $\phi_i : X_i \rightarrow S^1$ . We assume that  $\#X_i \ll \#X$  and we do not necessarily assume that any given  $x \in X$  is contained in many subsamples.

Our first step is to extend each coordinate  $\phi_i : X_i \rightarrow S^1$  to all of  $X$ . We extend  $\phi_i$  to a circular coordinate  $\tilde{\phi}_i : X \rightarrow S^1$  on all of  $X$  by a weighted average of  $\phi_i$  evaluated at points of  $X_i$ , using the *circular mean* for averaging. Modeling  $S^1$  as the unit circle in  $\mathbb{R}^2$ , we set

$$(4.2) \quad \tilde{\phi}_i(x) = \text{CircMean}(w, X_i, \phi_i, x) := \sum_{y \in X_i} w(x, y) \phi_i(y) \Big/ \left\| \sum_{y \in X_i} w(x, y) \phi_i(y) \right\|,$$

for  $x \notin X_i$ . Here  $w(x, y)$  is a weighting function; a standard choice is the Gaussian kernel  $w(x, y) = e^{-\beta \|x-y\|^2}$  for some  $\beta > 0$ . The circular mean is undefined when the sum inside the formula is zero and is unstable for values near zero. However, for a reasonable initial embedding  $\phi_i$ , points in  $X_i$  near any given point  $x$  land in a small interval of the circle and  $\beta$  could be chosen so that the resulting  $\tilde{\phi}_i(x)$  remains in that interval. In practice, we took  $\beta \approx \epsilon$ , where  $\epsilon$  is the scale parameter used in the density estimation procedure. In mild abuse of notation, we continue to denote these extensions by  $\phi_i : X \rightarrow S^1$ .

The next step is to find an approximate solution for the Procrustes problem on the circle for the images of the extended embeddings. This starts by leveraging solvers for the Euclidean Procrustes problem to approximate solutions in the circular case. Specifically, viewing  $S^1$  as a subset of  $\mathbb{R}^2$ , we solve the corresponding Procrustes problem for point clouds in  $\mathbb{R}^2$ , where the allowed transformations are restricted to rotations centered on the origin and reflections through a line through the origin, that is, elements of  $O(2)$ . Although these transformations send the unit circle to itself, and restricted to the unit circle are the same transformations we consider in the Procrustes problem on the circle (Definition 4.1), a solution to the



$O(2)$  Procrustes problem in  $\mathbb{R}^2$  does not necessarily give a solution to the circle version because (1) the points in the centroid found lie within but not necessarily on the circle, and (2) the metric on the circle in the loss function  $L$  of Definition 4.1 is the natural arclength metric and not the restriction of the metric on  $\mathbb{R}^2$ .

We address the first issue by forcing the centroid  $\Theta$  to lie on the circle by projecting back. Although numerically unlikely, it is possible that the origin may appear as one of the points in the  $\mathbb{R}^2$  centroid, and in this case it is a least squares minimization problem to choose the point for  $\Theta$  to be the one that minimizes the loss function. For the second issue, we have the following observation bounding the distances on the circle and distances in  $\mathbb{R}^2$  for a point on the circle and a point inside the circle projected back to the circle.

**Lemma 4.3.** *Let  $x, y$  be elements of the unit circle in  $\mathbb{R}^2$  and let  $r \in [0, 1]$ , then*

$$d_{S^1}(x, y) \leq \pi d_{\mathbb{R}^2}(x, ry)$$

As a consequence, we prove that a solution to the  $O(2)$  Procrustes problem in  $\mathbb{R}^2$  for configurations on  $S^1$  will be close to a solution to the Procrustes problem on the circle, depending on the optimal value of the loss function  $L$  of Definition 4.1.

**Proposition 4.4.** *Given  $k$  configurations of  $n$  points on the circle  $\Phi_1, \dots, \Phi_k$ , let  $((g_1, \dots, g_k), \Theta)$  be the solution to the generalized Procrustes problem on the circle, let  $((g'_1, \dots, g'_k), \Psi)$  be the solution to the  $O(2)$  Procrustes problem on  $\mathbb{R}^2$ , and let  $\Theta'$  be the projection of  $\Psi$  back to the circle as described above. Then*

$$\inf_{h \in O(2)} d(h \cdot \Theta, \Theta') \leq (1 + \pi) \sqrt{L^*},$$

where  $L^* = L((g_1, \dots, g_k), \Theta)$  is the minimum value of the generalized Procrustes loss on the circle.

*Proof.* For clarity, we subscript  $d$  with the symbol for the metric space to denote the respective distances. By the triangle inequality and the proposition above, we have

$$\begin{aligned} \inf_{h \in O(2)} d_{(S^1)^n}(h \cdot \Theta, \Theta') &= \inf_{h, h' \in O(2)} d_{(S^1)^n}(h \cdot \Theta, h' \cdot \Theta') \\ &\leq \inf_{h, h'} (d_{(S^1)^n}(h \cdot \Theta, \Phi_i) + d_{(S^1)^n}(h' \cdot \Theta', \Phi_i)) \\ &= \inf_{h, h'} (d_{(S^1)^n}(h \cdot \Phi_i, \Theta) + d_{(S^1)^n}(h' \cdot \Phi_i, \Theta')) \\ &= \inf_h d_{(S^1)^n}(h \cdot \Phi_i, \Theta) + \inf_h d_{(S^1)^n}(h \cdot \Phi_i, \Theta') \\ &\leq \inf_h d_{(S^1)^n}(h \cdot \Phi_i, \Theta) + \inf_h \pi d_{(\mathbb{R}^2)^n}(h \cdot \Phi_i, \Psi), \end{aligned}$$

where we use the  $\ell^2$  distances on the product metric spaces. Looking at these as coordinates for elements of  $\mathbb{R}^k$  (as  $i$  varies from 1 to  $k$ ), and applying the triangle

inequality in  $\mathbb{R}^k$ , we get

$$\begin{aligned}
(4.5) \quad \inf_h d_{(S^1)^n}(h \cdot \Theta, \Theta') &= \frac{1}{\sqrt{k}} \left( \sum_{i=1}^k \inf_h d_{(S^1)^n}(h \cdot \Theta, \Theta')^2 \right)^{1/2} \\
&\leq \frac{1}{\sqrt{k}} \left( \sum_{i=1}^k (\inf_h d_{(S^1)^n}(h \cdot \Phi_i, \Theta) + \inf_h \pi d_{(\mathbb{R}^2)^n}(h \cdot \Phi_i, \Psi))^2 \right)^{1/2} \\
&\leq \frac{1}{\sqrt{k}} \left( \sum_{i=1}^k \inf_h d_{(S^1)^n}(h \cdot \Phi_i, \Theta)^2 \right)^{1/2} + \frac{\pi}{\sqrt{k}} \left( \sum_{i=1}^k \inf_h d_{(\mathbb{R}^2)^n}(h \cdot \Phi_i, \Psi)^2 \right)^{1/2} \\
&= \left( \frac{1}{k} \sum_{i=1}^k \inf_h d_{(S^1)^n}(h \cdot \Phi_i, \Theta)^2 \right)^{1/2} + \pi \left( \frac{1}{k} \sum_{i=1}^k \inf_h d_{(\mathbb{R}^2)^n}(h \cdot \Phi_i, \Psi)^2 \right)^{1/2}
\end{aligned}$$

The first term on the last line is then  $\sqrt{L^*} = (L((g_1, \dots, g_k), \Theta))^{1/2}$ , since by hypothesis  $((g_1, \dots, g_k), \Theta)$  is the solution to the generalized Procrustes problem on the circle for the configurations  $\Phi_1, \dots, \Phi_k$ . For the second term, write  $L_{\mathbb{R}^2}$  for the Procrustes loss functional in  $\mathbb{R}^2$ ,

$$L_{\mathbb{R}^2}((h_1, \dots, h_k), \Xi) := \frac{1}{k} \sum_{i=1}^k \sum_{j=1}^n d_{\mathbb{R}^2}(h_i \cdot \Phi_i(j), \Xi(j))^2 = \frac{1}{k} \sum_{i=1}^k d_{(\mathbb{R}^2)^n}(h_i \cdot \Phi_i, \Xi)^2.$$

Since  $((g'_1, \dots, g'_k), \Psi)$  is the solution to the  $O(2)$  Procrustes problem in  $\mathbb{R}^2$  for the configurations  $\Phi_1, \dots, \Phi_k$ , we have that

$$\frac{1}{k} \sum_{i=1}^k \inf_h d_{(\mathbb{R}^2)^n}(h \cdot \Phi_i, \Psi)^2 = L_{\mathbb{R}^2}((g'_1, \dots, g'_k), \Psi) \leq L_{\mathbb{R}^2}((g_1, \dots, g_k), \Theta)$$

and since the standard and Euclidean metrics on the circle satisfy  $d_{\mathbb{R}^2} \leq d_{S^1}$ , we have

$$L_{\mathbb{R}^2}((g_1, \dots, g_k), \Theta) \leq L((g_1, \dots, g_k), \Theta) = L^*.$$

Plugging these inequalities back into (4.5), we get the inequality in the statement.  $\square$

The purpose of the approximate solution using the  $O(2)$  Procrustes problem in  $\mathbb{R}^2$  is that solvers for this problem use non-local methods, which can jump out of basins of attraction to which local methods like hill climbing are confined. This is key because  $O(2)^k$  is not connected and the error surface of the loss function is not convex within connected regions. However, once we have an approximate solution with an exact solution nearby, hill climbing methods then can effectively zero in on the exact solution.

Our algorithm starts with an approximate solution from the  $O(2)$  Procrustes problem in  $\mathbb{R}^2$ , constructed for example using the algorithm of ten Berge [4, p. 272] as a seed position to start hill climbing. Then, we hill climb by iteratively rotating according to a learning rate schedule (i.e., a decreasing function of the iteration number) each of the input configurations as well as each point in the candidate centroid, choosing among the clockwise, counterclockwise, or no rotation for each configuration and each point of the candidate centroid giving the smallest value for the loss function. We terminate and return the candidate centroid when some

convergence criterion is met (e.g., the change in the loss function falls below a pre-defined threshold).

We summarize our algorithm as follows:

**Input:** A data set  $X \subset \mathbb{R}^N$ , subsamples  $X_i \subset X$ , and circular coordinates  $\phi_i: X_i \rightarrow S^1$  for  $i = 1, \dots, k$ .

**Step 1:** Extend each  $\phi_i$  to a function  $\Phi_i: X \rightarrow S^1$  using the circular mean: for  $x \in X_i$  define  $\Phi_i(x) = \phi_i(x)$  and for  $x \notin X_i$ , define  $\Phi_i(x) = \text{CircMean}(w, X_i, \phi_i, x)$  (see (4.2) and text following for description).

**Step 2:** Solve the  $O(2)$  Procrustes problem in  $\mathbb{R}^2$  for the configurations  $\Phi_1, \dots, \Phi_k$  via the ten Berge algorithm to produce rotation/reflection guesses  $g_1, \dots, g_k$  and a centroid configuration  $\Theta$  obtained by radially projecting the centroid obtained in  $\mathbb{R}^2$  back to the circle.

**Step 3:** Use hill climbing starting at these guesses to search for local minima for the loss function  $L$  in Definition 4.1.

**Step 4:** Return the final centroid configuration.

## 5. EXPERIMENTAL RESULTS

We undertook several experiments with both synthetic and real-world data to test the effectiveness of the algorithm. In subsection 5.1, we illustrate with synthetic data what goes wrong with circular coordinates derived from unevenly sampled data and observe that the algorithm corrects the coordinates. In subsection 5.2, we review two sets of real-world data on neuronal recordings from *C. elegans*. In the first set of these results, we used our algorithm to re-analyze the dataset from Kato et al. [22] on the relationship of locomotory behavior to recurrent trajectories in neuronal phase space. In the second set, we analyzed recent data from Yemini et al. [46] on the response of worms to various sensory stimuli.

For each experiment, we computed and compared two coordinates: the global “uncorrected coordinate” obtained by calculating a single circular coordinate on the data without subsampling and the “corrected coordinate” obtained from our proposed approach of subsampling, aligning, and averaging coordinates.

**5.1. Unbalanced circles and ellipses.** To illustrate what can go wrong with circular coordinates for an uneven density, we generated a synthetic unbalanced circle data set as follows. The data set consists of 1000 independently generated points in  $\mathbb{R}^2$ , where the distance from the origin to each point is normally distributed with mean 1 and standard deviation 0.1 and the angles that these vectors make with the positive  $x$ -axis are drawn from a von Mises distribution with dispersion 1.3. This produces samples concentrated around the unit circle with a denser region near the angle  $0 = 2\pi$  radians. Producing circular coordinates heavily overweights the denser region; see Figure 1.

Density-based subsampling drastically improves the obtained coordinate in this artificial example. Using the count density estimator  $\hat{\rho}_\epsilon$  for  $\epsilon$  chosen according to Scott’s rule, we generated 30 density-equalized subsamples with expected size 50. Then, we used persistent cohomology to find circular coordinates and used generalized orthogonal Procrustes alignment to obtain the corrected coordinate. The results are shown in the bottom row of Figure 1. The agreement between the true angle and the inferred angle is much better in this case.

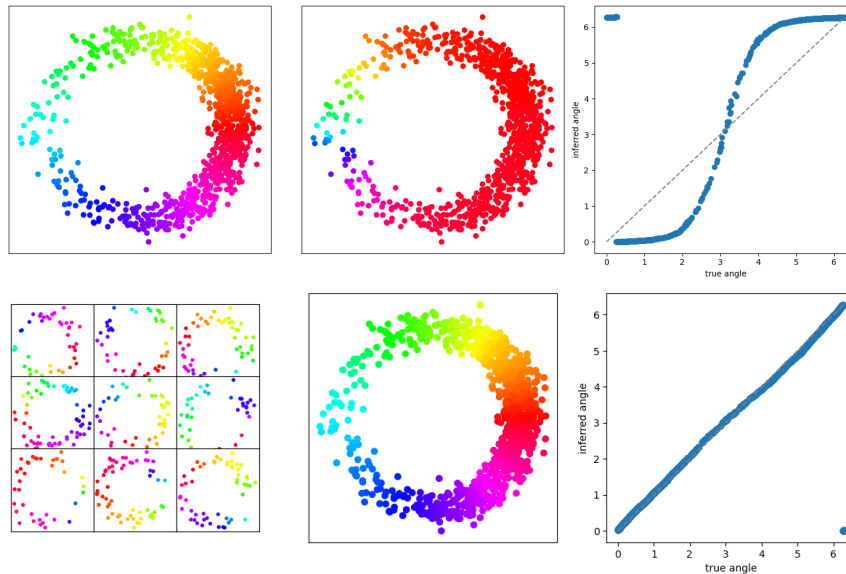


FIGURE 1. Top: An unbalanced circle dataset colored by the “true” angle (left) or the uncorrected coordinate inferred from persistent cohomology (center). A plot of the uncorrected coordinate against the true coordinate (right); the dotted diagonal line indicates equality. Bottom: Examples of the subsampled unbalanced circle and their inferred phases (left), the final corrected coordinate obtained by aligning the coordinates assigned to subsamples (center), and a plot of the corrected coordinate against the true coordinate (right).

Next, we considered less symmetric examples where the reach of the manifold becomes involved: unbalanced ellipses that are denser near one vertex. The procedure for generating these point clouds is the same for the unbalanced circle, except that we applied a dilation factor of 1.6 in the  $x$  direction; see the top row of Figure 2. The inferred coordinate does not recover the arc length exactly, but nonetheless we still see a significant improvement using the corrected coordinates. See the bottom row of Figure 2.

## 5.2. *C. elegans* neuronal recordings.

5.2.1. *Data from Kato et al.* We used our method to construct coordinates on the neuronal activity phase space of the nematode *C. elegans*. The Kato et al. dataset [22] recorded multivariate time series with features corresponding to the calcium traces of a subset of neurons sampled at a particular frequency. The animals were transgenically designed so that the neuron centers fluoresce upon calcium influx, which is a proxy for neuronal activation. The original analysis found that the different regions of the phase space extracted from this high-dimensional data reflect the different states of the worm locomotory gait, termed *sinusoids* or *pirouettes*. The worm cycles through these different states as it executes its motor commands;

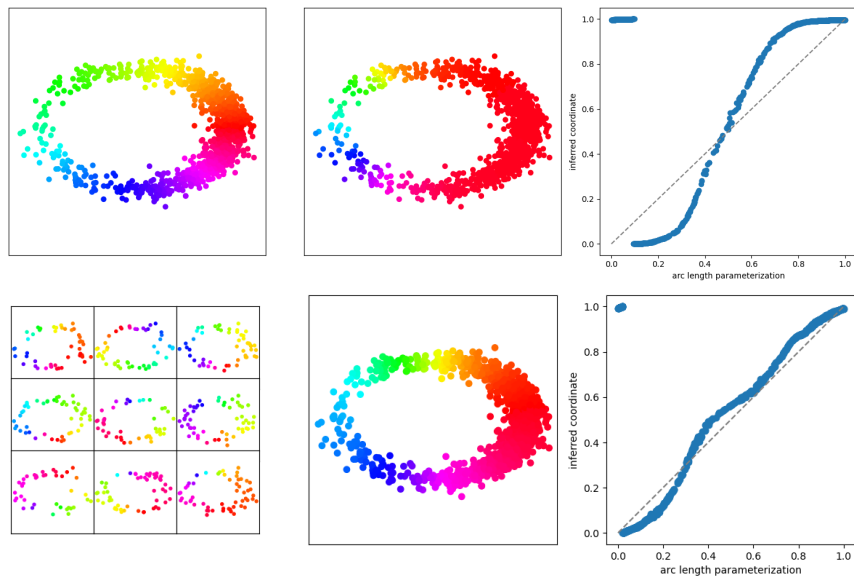


FIGURE 2. Top: An unbalanced ellipse dataset colored by arc length (left) or the uncorrected coordinate inferred from persistent cohomology (center). A plot of the uncorrected coordinate against the arc length parametrization (right). Bottom: Examples of the subsampled unbalanced ellipse and their inferred phases (left), the final corrected coordinate (center), and a plot of the corrected coordinate against the arc length parametrization (right).

in particular, the underlying dynamical system is recurrent and we expect the trajectories to consist of loops in the phase space.

Several methods have been applied to study these non-stationary and high-dimensional neuronal activity trajectories, including adaptive locally linear segmentation [14], hierarchical recurrent state space models [25], asymmetric diffusion mapping [10, 9], dynamic mode decomposition with control [17], and nonlinear control [29]. Beyond a general qualitative description, a quantitative model of the different states of the worm neuronal manifold – continuous or discrete – is a preliminary step to understand inter-state transitions and to generate testable hypotheses about the underlying biological mechanisms that drive and control the dynamical system and the external factors that may alter it.

As validation of our method, we applied it to recover these recurrent patterns and more from the *C. elegans* neuronal activity data in a flexible manner and perform nonlinear continuous state space segmentation. TDA methods have been previously used to study the activity of neuron ensembles, for example, in head direction cells [39] or in grid cells [19] in mice. Our analysis demonstrates that these techniques are also applicable to study whole-brain recordings (as opposed to specific groups of neurons with spatial-processing function) of an invertebrate nervous system. Furthermore, in this case the manifold of interest has no direct physical interpretation like head direction or allocentric location, but rather is an abstract representation of brain state.

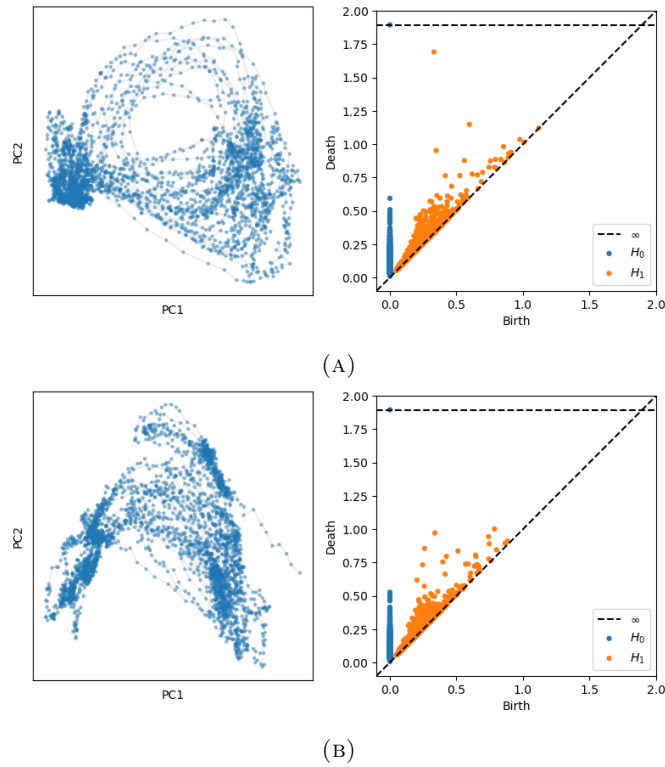


FIGURE 3. The projection of the neuronal trajectories into PCA space (left) and the persistence diagram (right) for two different worms.

We reproduced the dimensionally-reduced version of the phase space from [22]. More specifically, by phase space here we mean a combination of all the available activity traces and their derivatives obtained through total-variation regularization. Then, we examined the persistent cohomology results to determine the general global shape of the phase space. For instance, for the worm neuronal trajectory depicted in Figure 3(a), we see that there is an obvious large loop that is confirmed by a long-lived class in  $PH^1$  with late death time, which we deem suitable for further coordinatization. On the other hand, for the worm neuronal trajectory shown in Figure 3(b), we do not detect a clear persistent large loop but rather multiple smaller loops, which suggests that the shape should be modeled differently: imposing a circular coordinate onto the data in its current form is unlikely to be effective. This is not to say that this worm is definitely not exhibiting the expected cyclic locomotory brain patterns, but that additional preprocessing of the data is perhaps needed. This shows one of the advantages of our TDA approach, which separates the problem of shape detection from shape coordinatization. While other methods assume – correctly or not – prior knowledge about the general shape of neuronal trajectories, we can first detect loops in the data *prior* to finding coordinates for them (if they exist).

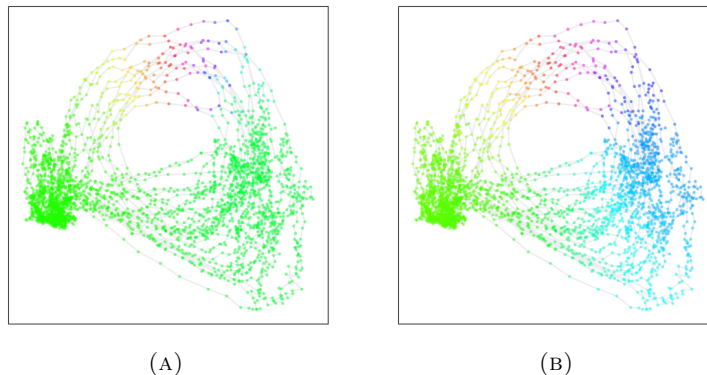


FIGURE 4. The neuronal manifold of *Caenorhabditis elegans* global brain dynamics, coordinatizing a cyclic locomotory gait, colored by (a) the uncorrected coordinate or (b) the corrected coordinate.

For the phase space of the first worm above with the long-lived cohomology class, we calculated the uncorrected and corrected circular coordinates; see Figure 4. By visual inspection, the uncorrected coordinate concentrates more of the phase changes near the top of the loop and less near the bottom, whereas the corrected coordinate equalize the size of the phases. Note that the density imbalance that arises here is not a mere sampling error but a natural real-life consequence of the brain state prior to the worm’s decision to start turning.

For this data set, we also have annotations into discrete brain states provided in the original article, which were obtained by examining the trace of a single command interneuron (AVAL) and manually setting thresholds. Figure 5 compares the continuous coordinates inferred using our approach with the original annotations by plotting the coordinates in the tangent bundle  $TS^1 \cong S^1 \times \mathbb{R}$  as a polar plot; the tangent vectors were obtained from numerically differentiating the coordinates. Overall, we see coordinate values from the same state are clustered together, which demonstrates agreement between the new and old results. This shows that our algorithm recovers the model of the brain state manifold proposed in [22], c.f. Figure 4(E) in that paper. We also see that the uncorrected coordinate tends to obscure the smaller loop corresponding to ventral turns, whereas the corrected coordinate manages to recover this second loop more clearly.

**5.2.2. Data from Yemini et al.** We also applied our methods to the more recent, more expansive *C. elegans* recordings obtained from Yemini et al. [46]. These are calcium trace recordings of approximately four minutes in length per animal, sampled at 4 Hz. In contrast to the recordings analyzed in [22], over a hundred neurons were recorded simultaneously with individual resolution. Furthermore, the animals being recorded are subjected to various olfactory and gustatory stimuli at minute intervals during the experiment. The rapid changes in the environment relative to the short durations of the recordings complicate the analysis, but we nonetheless show that the locomotory cycles can still be recovered using our methods.

To create a phase space from the raw data, we deployed techniques that are commonly used to analyze time series from dynamical systems. We took advantage

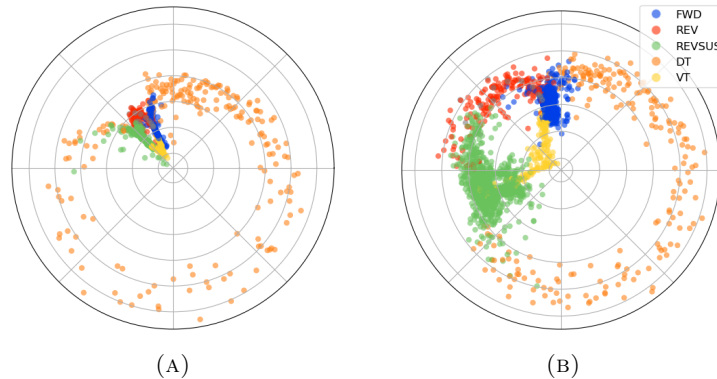


FIGURE 5. Comparison between the labels from [22] and our inferred coordinates, either (a) uncorrected or (b) corrected. Points are colored according to the discrete categories of the provided labels: forward (FWD), reversal (REV), sustained reversal (REVSUS), dorsal turn (DT), and ventral turn (VT).

of the fact that the identities of the neurons in this experiment are individually resolved and restricted to a few specific neurons of interest; we focus on the command interneuron classes AVA and AVB whose activities have been found to reflect various stages of the nematode locomotory pattern. These neurons are located downstream of most sensory neurons in the olfactory and gustatory circuits and upstream of motor neurons that control the muscles in the worm, and are known to be hubs for sensorimotor integration. First, we detrended the data by removing mean and scale fluctuations against a moving average background. Second, we created a delay embedding of the data, i.e., we mapped an observation function  $f: [0, T] \rightarrow \mathbb{R}^N$  to its various lagged values:

$$S_{d,\tau}f: t \mapsto (f(t), f(t + \tau), \dots, f(t + d\tau)).$$

The rationale for doing so comes from *Takens' embedding theorem* [44], which roughly asserts that the topology of an attractor of a dynamical system can be recovered from a suitable delay embedding of an observation function. For instance, if we take  $d = \tau = 1$ , then  $S_{1,1}f$  has the same span as the function evaluated at the original times together with its first differences – in other words, the phase space we are constructing is a generalization of the phase space built using function values and derivatives. We took  $d = 4$  and  $\tau = 20$  frames (roughly 5 seconds), but our results are robust with respect to these choices. Finally, as the Takens embedding is typically very high-dimensional, we performed linear PCA to reduce the number of dimensions to 5.

We present our results in Figure 6, which displays the phase spaces for six worms, colored by the uncorrected and corrected coordinates. The uncorrected coordinates are slightly noisier and less even; see the quantitative discussion in the next section for more measures of improvement. We again recover coordinates which correspond to observed worm behaviors.

**5.3. Qualitative evaluation in terms of mutual information.** We propose an intrinsic criterion for evaluating the coordinates we produce. With real-world



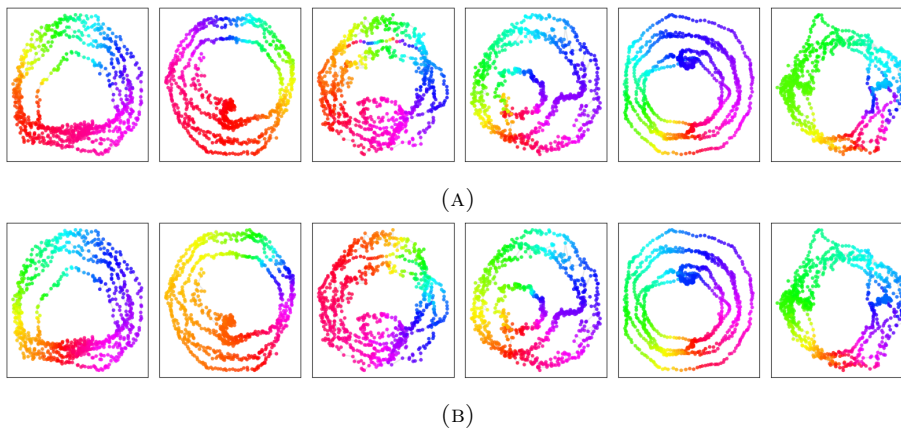


FIGURE 6. *C. elegans* neuronal manifolds constructed for six worms from [46], colored by (a) the uncorrected coordinate and (b) the corrected coordinate.

data sets, we do not typically have access to “ground truth”. We could compare our results to expert-annotated labels as we did for the Kato et al. dataset, but these are not always available, as in the case for the Yemini et al. dataset. Instead, we can quantify the association or correlation of a coordinate with respect to the position in the full phase space using *mutual information*, which we briefly review.

Let  $(X, Y)$  be a pair of continuous random variables with support  $\mathcal{X} \times \mathcal{Y}$ , joint density  $p_{(X,Y)}(x, y)$ , and marginal densities  $p_X(x)$  and  $p_Y(y)$ . Then the mutual information between  $X$  and  $Y$  is defined as

$$I(X, Y) = \int_{\mathcal{X} \times \mathcal{Y}} p_{(X,Y)}(x, y) \cdot \log \frac{p_{(X,Y)}(x, y)}{p_X(x)p_Y(y)} dx dy.$$

Equivalently, mutual information can be defined in terms of entropy:

$$I(X, Y) = H(X) - H(X | Y) = H(Y) - H(Y | X),$$

i.e.,  $I(X, Y)$  is the reduction of uncertainty in  $X$  once  $Y$  is known, or vice versa. If  $X$  and  $Y$  are independent, then  $I(X, Y) = 0$ . Furthermore, if  $(X, Y)$  is a bivariate Gaussian random variable, we have  $I(X, Y) = -\frac{1}{2} \log(1 - \rho^2)$ , where  $\rho$  is the correlation between  $X$  and  $Y$ . This shows that mutual information is a form of nonlinear correlation between random variables.

Kraskov, Stögbauer, and Grassberger [23] proposed a method to estimate  $I(X, Y)$  from  $N$  iid samples of  $(X, Y)$  based on nearest neighbors. Fix a positive integer  $k$  (we set  $k = 3$  below), and consider the sup-metric on  $\mathcal{X} \times \mathcal{Y}$ . For each observation  $(x, y)$ , consider the smallest rectangle centered at  $(x, y)$  that contains the  $k$  nearest neighbors of  $(x, y)$  according to the sup-metric; let the dimensions of this rectangle be  $\epsilon_x$  and  $\epsilon_y$ . Let  $n_x$  be the number of other points  $(x', y')$  with  $d(x, x') \leq \frac{\epsilon_x}{2}$ , and let  $n_y$  be the number of other points  $(x', y')$  with  $d(y, y') \leq \frac{\epsilon_y}{2}$ . Then the *KSG estimator* of the mutual information is given by

$$\hat{I}(X, Y) = \psi(k) - \frac{1}{k} - \frac{1}{N} \sum_{(x,y)} (\psi(n_x) + \psi(n_y)) + \psi(N).$$

While in principle the mutual information  $I(X, Y)$  can be unbounded above, the KSG estimator is bounded above:

$$\hat{I}(X, Y) \leq \hat{I}_{\max} = \psi(N) - \psi(k) - \frac{1}{k}$$

since  $n_x, n_y \geq k$ . Equality is attained when  $n_x = n_y = k$ , i.e., the  $k$ -nearest neighbors of a point are exactly the same whether they are computed in  $X$  or in  $Y$ . This gives an additional reason why  $\hat{I}$  can be used to evaluate the concordance of two variables. In order to standardize the values of the estimator  $\hat{I}$  across datasets, we normalize it by its maximum value and calculate

$$\hat{I}_{\text{norm}}(X, Y) = \frac{\hat{I}(X, Y)}{\hat{I}_{\max}}$$

instead. Note that there are several other definitions of normalized mutual information in the literature, but  $\hat{I}_{\text{norm}}$  is *not* one of them: it is simply a convenient normalization specific to the KSG estimator. For more information on other normalized mutual information estimators, see [30].

Observe that the KSG estimator depends only on the metrics on  $X$  and  $Y$ . Returning to our experiments, let  $X$  be the dataset equipped with the Euclidean metric, and let  $Y$  be the same dataset, but with the metric induced by a circular coordinate. Different circular coordinates give rise to different mutual information values. The data processing inequality implies that information is necessarily lost when we perform dimensionality reduction, but a higher mutual information means that more of the structure of the original dataset is retained by the coordinate.

To validate the use of KSG estimator to evaluate various circular coordinates, we first applied it to the setup of the synthetic circle data from above. We generated 20 replicates of the unbalanced circle (with the same parameters), extracted the uncorrected circular coordinate and the corrected circular coordinate for each, and computed their mutual information with the true coordinate. The results are shown in Figure 7(a), where we see that the mutual information of the corrected circular coordinate is significantly higher than the uncorrected circular coordinate.

Next, we turn to the worm neuronal activity data from Kato et al. (Figure 7(b)) and Yemini et al. (Figure 7(c)). While the mutual information estimates are now further from their maximum possible value, we nonetheless see that the corrected coordinate from our approach yields higher mutual information values than the uncorrected coordinate in every case. This demonstrates that our subsample, align, and average method produces more informative coordinates and captures more of the geometry of the original data than using uncorrected coordinates in real-world data.

**5.4. Runtime analysis.** Finally, we briefly demonstrate the time savings of our algorithm. Basically, computing persistent cohomology and extracting circular coordinates amounts to matrix manipulations which have superlinear time complexity in the number of points (e.g., see [27, 28] which shows that persistent (co)homology and (co)cycles can be computed in matrix multiplication time, asymptotically). Therefore, by splitting the dataset into smaller pieces and then computing and averaging persistent cohomology coordinates on the subsamples, we may be able to obtain considerable decreases in runtime. See also the recent work [31] which explains how to efficiently parallelize the distributed computation of persistent cohomology.

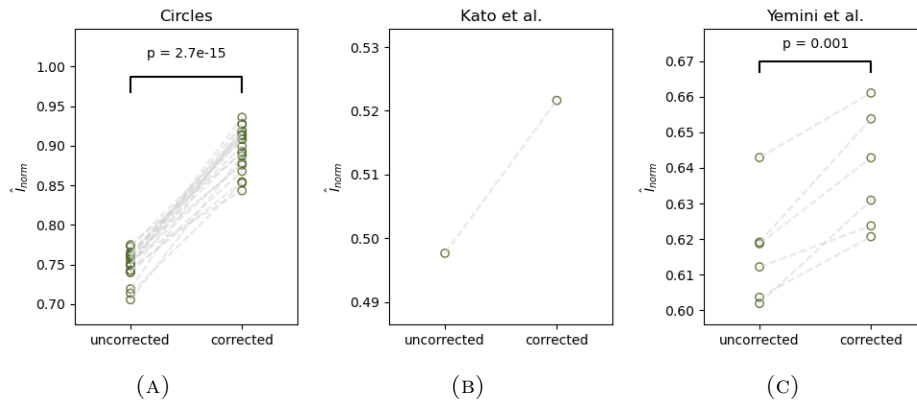


FIGURE 7. Estimates of mutual information for (a) the unbalanced circle, (b) the worm from Kato et al., and (c) the six worms from Yemini et al. Where displayed, the  $p$ -values are calculated from an one-sided paired  $t$ -test.

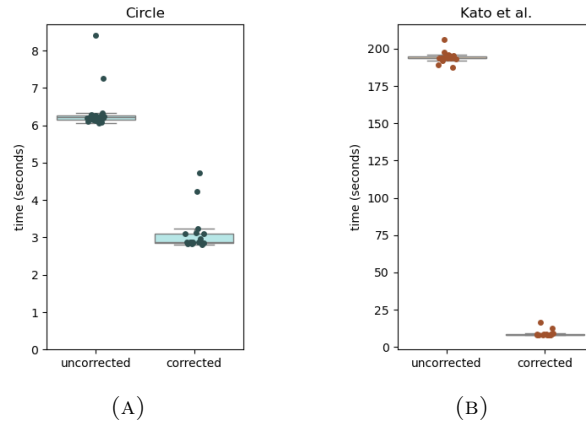


FIGURE 8. Time taken to compute the uncorrected and corrected circular coordinates respectively, with 20 replicates in two datasets.

To demonstrate this in practice, we timed the execution of the direct approach of computing the uncorrected and the corrected coordinate on two of the datasets described above: the synthetic circle dataset (1000 points) and the Kato et al. *C. elegans* neuronal activity dataset (3021 time points). Each of these timing experiments were repeated 20 times, and the results are displayed in Figure 8.

For the circle dataset, the minimum runtime over 20 repeats for computing the corrected circular coordinate is 2.80 seconds, compared with 6.05 seconds for the uncorrected circular coordinate, which is a  $2.16\times$  runtime reduction. For the worm dataset, the minimum runtime for the corrected circular coordinate is 8.17 seconds, compared with 188 seconds for the uncorrected circular coordinate, which is a  $23.0\times$  reduction. This indicates that not only is the subsampling approach more time-efficient even with the extra alignment steps but also the time savings

scales with the size of the datasets, which is important as the datasets that are generated nowadays are often very large. Our approach is well-equipped to handle these big datasets; indeed, by processing the data in smaller chunks we may be able to analyze datasets that could not be analyzed entirely within a single run at all.

## 6. DISCUSSION

In this paper, we introduced a new algorithm for finding robust circular coordinates on data that is expected to exhibit recurrence. Our algorithm has three main steps: first, it uses rejection sampling to correct for inhomogeneous sampling; second, it extracts the coordinates from persistent cohomology; and finally, it applies Procrustes matching to align and average the coordinates. In experimental and synthetic data, this subsampling and averaging approach produced coordinates which are robust to noise and outliers and is significantly more efficient than simply applying persistent cohomology to the entire data set. Our method is also stable by design, which is an essential desideratum for unsupervised data analysis.

There are a number of theoretical questions we intend to explore in future work. For one thing, the success of our algorithm raises questions about geometries other than the circle for capturing behavior of dynamical systems. The circle is an obvious place to start both because of its simplicity as well as its direct connection to dimension 1 cohomology, but there are many other simple model manifolds that could be worth exploring [35, 40]. For another, there remain many qualitative and quantitative questions about robustness properties and the precise way our algorithm interacts with noise. Finally, we do not understand the local convexity and global properties of the optimization problem that arises when solving for the Procrustes alignment. Although in practice our algorithm converges rapidly and is stable with respect to random jitter, it would be desirable to have formal guarantees.

There are also many interesting scientific questions that arise from the experimental studies. The analysis of neuronal activity recordings revealed a topological model of neuronal trajectories for *C. elegans* that is constructed from loops in which different regions of the brain state space can be mapped to specific and interpretable macroscopic behaviors in the worm. Many questions arise about these trajectories on the neuronal manifold:

- How universal or conserved are neuronal activity patterns – in what ways does it vary between individual animals, or across various behavioral modes or environmental stimuli?
- To what extent are future brain states predictable starting from an initial state?
- What are the neuronal units and circuits that support the activity patterns we observe?

Using circular coordinates inferred from *C. elegans* data, our results confirm the locomotory cycle is highly conserved across subjects and predictable to the extent that neuronal activity is recurrent. While this may be obvious in our simplified model system, for more complicated and higher-dimensional circuits it is essential to have an unsupervised framework that can operate in the high-dimensional ambient spaces of simultaneous recordings of thousands of neurons or millions of voxels.

A next step would be to explore how the presentation of different stimuli is picked up by the sensory apparatus and integrated by decision-making circuits that output motor commands, thereby changing the normal progression through the

cycle. Separately, given the prominence of the circular trajectories, it would also be interesting to search for other phenomena and novel patterns that are orthogonal to them in the neuronal activity of *C. elegans* [1]. In the data we analyzed this neuronal circuit is more or less known since we are studying recurrent locomotory behavior; in general one can search for neural subunits that generate interesting coordinates.

Finally, all of these questions have analogues in many other neural systems; for example, it would be interesting to understand whether qualitatively similar conservation and decision-making processes occur in animals such as flies and mice.

## REFERENCES

- [1] Nils A. Baas. “On the concept of space in neuroscience”. In: *Current Opinion in Systems Biology* 1 (2017), pp. 32–37. DOI: 10.1016/j.coisb.2016.12.002.
- [2] Mikhail Belkin and Partha Niyogi. “Towards a theoretical foundation for Laplacian-based manifold methods”. In: *Journal of Computer and System Sciences* 74.8 (2008), pp. 1289–1308. DOI: 10.1016/j.jcss.2007.08.006.
- [3] Clément Berenfeld and Marc Hoffmann. “Density estimation on an unknown submanifold”. In: *Electronic Journal of Statistics* 15.1 (2021), pp. 2179–2223.
- [4] Jos M. F. ten Berge. “Orthogonal Procrustes rotation for two or more matrices”. In: *Psychometrika* 42.2 (1977), pp. 267–276.
- [5] Mira Bernstein, Vin De Silva, John C. Langford, and Joshua B. Tenenbaum. “Graph Approximations to Geodesics on Embedded Manifolds”. In: (2000).
- [6] Gérard Biau, Frédéric Chazal, David Cohen-Steiner, Luc Devroye, and Carlos Rodríguez. “A weighted  $k$ -nearest neighbor density estimate for geometric inference”. In: *Electronic Journal of Statistics* 5 (2011), pp. 204–237. DOI: 10.1214/11-EJS606.
- [7] Andrew J. Blumberg, Mathieu Carriere, Jun Hou Fung, and Michael A. Mandell. “Resampling and averaging coordinates on data”. 2024. arXiv: 2408.01379 [stat.ML]. URL: <https://arxiv.org/abs/2408.01379>.
- [8] Jean-Daniel Boissonnat, André Lieutier, and Mathijs Wintraecken. “The reach, metric distortion, geodesic convexity and the variation of tangent spaces”. In: *Journal of Applied and Computational Topology* 3.1 (2019), pp. 29–58. DOI: 10.1007/s41468-019-00029-8.
- [9] Connor Brennan, Adeeti Aggarwal, Rui Pei, David Sussillo, and Alex Proekt. “One dimensional approximations of neuronal dynamics reveal computation strategy”. In: *PLOS Computational Biology* 19.1 (2023), pp. 1–27. DOI: 10.1371/journal.pcbi.1010784.
- [10] Connor Brennan and Alexander Proekt. “A quantitative model of conserved macroscopic dynamics predicts future motor commands”. In: *eLife* 8 (2019). DOI: 10.7554/eLife.46814.
- [11] Gunnar Carlsson. “Topological methods for data modelling”. In: *Nature Reviews Physics* 2 (12 2020), pp. 697–708. DOI: 10.1038/s42254-020-00249-3.
- [12] Frédéric Chazal, David Cohen-Steiner, and Quentin Mérigot. “Geometric inference for probability measures”. In: *Foundations of Computational Mathematics* 11.6 (2011), pp. 733–751.

- [13] Frédéric Chazal, Vin de Silva, Marc Glisse, and Steve Oudot. *The structure and stability of persistence modules*. Springer-Verlag, 2016.
- [14] Antonio C. Costa, Tosif Ahamed, and Greg J. Stephens. “Adaptive, locally linear models of complex dynamics”. In: *Proceedings of the National Academy of Sciences* 116.5 (2019), pp. 1501–1510. DOI: 10.1073/pnas.1813476116.
- [15] Luc Devroye. *A Course in Density Estimation*. Vol. 14. Progress in Probability and Statistics. Birkhauser, 1987.
- [16] Herbert Edelsbrunner and John Harer. *Computational topology: an introduction*. American Mathematical Society, 2010.
- [17] Charles Fieseler, Manuel Zimmer, and J. Nathan Kutz. “Unsupervised learning of control signals and their encodings in *Caenorhabditis elegans* whole-brain recordings”. In: *Journal of The Royal Society Interface* 17.173 (2020). DOI: 10.1098/rsif.2020.0459.
- [18] Evelyn Fix and J. L. Hodges. “Discriminatory Analysis. Nonparametric Discrimination: Consistency Properties”. In: *International Statistical Review / Revue Internationale de Statistique* 57.3 (1989), pp. 238–247. DOI: 10.2307/1403797.
- [19] Richard J. Gardner, Erik Hermansen, Marius Pachitariu, Yoram Burak, Nils A. Baas, Benjamin A. Dunn, May-Britt Moser, and Edvard I. Moser. “Toroidal topology of population activity in grid cells”. In: *Nature* 602.7895 (2022), pp. 123–128. DOI: 10.1038/s41586-021-04268-7.
- [20] Robert Ghrist. “Barcodes: The persistent topology of data”. In: *Bull. Amer. Math. Soc.* 45 (2008), pp. 61–75.
- [21] Abigail Hickok. “A Family of Density-Scaled Filtered Complexes”. arXiv:2112.03334. 2021.
- [22] Saul Kato, Harris S. Kaplan, Tina Schrödel, Susanne Skora, Theodore H. Lindsay, Eviatar Yemini, Shawn Lockery, and Manuel Zimmer. “Global Brain Dynamics Embed the Motor Command Sequence of *Caenorhabditis elegans*”. In: *Cell* 163 (3 2015), pp. 656–669. DOI: 10.1016/j.cell.2015.09.034.
- [23] Alexander Kraskov, Harald Stögbauer, and Peter Grassberger. “Estimating mutual information”. In: *Phys. Rev. E* 69 (6 2004), p. 066138. DOI: 10.1103/PhysRevE.69.066138.
- [24] Mike Lesnick. “Studying the Shape of Data Using Topology”. 2013. URL: <https://www.ias.edu/ideas/2013/lesnick-topological-data-analysis>.
- [25] Scott Linderman, Annika Nichols, David Blei, Manuel Zimmer, and Liam Paninski. “Hierarchical recurrent state space models reveal discrete and continuous dynamics of neural activity in *C. elegans*”. In: *bioRxiv* (2019). DOI: 10.1101/621540.
- [26] D. O. Loftsgaarden and C. P. Quesenberry. “A Nonparametric Estimate of a Multivariate Density Function”. In: *The Annals of Mathematical Statistics* 36.3 (1965), pp. 1049–1051. DOI: 10.1214/aoms/1177700079.
- [27] Nikola Milosavljević, Dmitriy Morozov, and Primoz Skraba. “Zigzag persistent homology in matrix multiplication time”. In: *Proceedings of the Twenty-Seventh Annual Symposium on Computational Geometry*. New York, NY, USA: Association for Computing Machinery, 2011, pp. 216–225. DOI: 10.1145/1998196.1998229.

- [28] Dmitriy Morozov and Primoz Skraba. “Persistent (Co)Homology in Matrix Multiplication Time”. arXiv:2412.02591. 2024.
- [29] Megan Morrison, Charles Fieseler, and J. Nathan Kutz. “Nonlinear Control in the Nematode *C. elegans*”. In: *Frontiers in Computational Neuroscience* 14 (2021). DOI: 10.3389/fncom.2020.616639.
- [30] Daniel Nagel, Georg Diez, and Gerhard Stock. “Accurate estimation of the normalized mutual information of multidimensional data”. arXiv:2405.04980. 2024.
- [31] Arnur Nigmatov and Dmitriy Morozov. “Distributed Computation of Persistent Cohomology”. arXiv:2410.16553. 2024.
- [32] Steve Oudot. *Persistence theory: from quiver representations to data analysis*. American Mathematical Society, 2015.
- [33] Taejin Paik and Jaemin Park. “Circular Coordinates for Density-Robust Analysis”. In: (2023). arXiv: 2301.12742. URL: <https://arxiv.org/abs/2301.12742>.
- [34] Emanuel Parzen. “On Estimation of a Probability Density Function and Mode”. In: *The Annals of Mathematical Statistics* 33.3 (1962), pp. 1065–1076. DOI: 10.1214/aoms/1177704472.
- [35] Jose A. Perea. “Multiscale Projective Coordinates via Persistent Cohomology of Sparse Filtrations”. In: *Discrete Computational Geometry* 59 (2018), pp. 175–225. DOI: 10.1007/s00454-017-9927-2.
- [36] Jose A. Perea. “Sparse Circular Coordinates via Principal  $\mathbb{Z}$ -Bundles”. In: *Topological Data Analysis. Abel Symposia*. Ed. by Nils A. Baas, Gunnar E. Carlsson, Gereon Quick, Markus Szymik, and Marius Thauale. Vol. 15. Springer, Cham, 2020, pp. 435–458. DOI: 10.1007/978-3-030-43408-3\_17.
- [37] Raul Rabadan and Andrew J. Blumberg. *Topological Data Analysis for Genomics and Evolution: Topology in Biology*. Cambridge University Press, 2019. DOI: 10.1017/9781316671665.
- [38] Murray Rosenblatt. “Remarks on Some Nonparametric Estimates of a Density Function”. In: *The Annals of Mathematical Statistics* 27.3 (1956), pp. 832–837. DOI: 10.1214/aoms/1177728190.
- [39] Erik Rybakken, Nils Baas, and Benjamin Dunn. “Decoding of Neural Data Using Cohomological Feature Extraction”. In: *Neural Computation* 31.1 (2019), pp. 68–93. DOI: 10.1162/neco\_a\_01150.
- [40] Nikolas C. Schonsheck and Stefan C. Schonsheck. “Spherical coordinates from persistent cohomology”. In: *Journal of Applied and Computational Topology* 8 (2024), pp. 149–173. DOI: 10.1007/s41468-023-00141-w.
- [41] David W. Scott. *Multivariate Density Estimation: Theory, Practice and Visualization*. John Wiley & Sons, 2015.
- [42] Vin de Silva, Dmitriy Morozov, and Mikael Vejdemo-Johansson. “Persistent Cohomology of Circular Coordinates”. In: *Discrete & Computational Geometry* 45.4 (2011), pp. 737–759. DOI: 10.1007/s00454-011-9344-x.
- [43] Elchanan Solomon, Alexander Wagner, and Paul Bendich. “From Geometry to Topology: Inverse Theorems for Distributed Persistence”. In: *38th International Symposium on Computational Geometry (SoCG 2022)*. Ed. by Xavier Goaoc and Michael Kerber. Vol. 224. Leibniz International Proceedings in Informatics (LIPIcs). Dagstuhl, Germany: Schloss Dagstuhl – Leibniz-Zentrum für Informatik, 2022, 61:1–61:16. DOI: 10.4230/LIPIcs.SocG.2022.61.

- [44] Floris Takens. “Detecting strange attractors in turbulence”. In: *Dynamical Systems and Turbulence, Warwick 1980*. Ed. by David Rand and Lai-Sang Young. Springer Berlin Heidelberg, 1981, pp. 366–381. DOI: 10.1007/BFb0091924.
- [45] Mikael Vejdemo-Johansson, Florian T. Pokorny, Primoz Skraba, and Danica Kragic. “Cohomological learning of periodic motion”. In: *Applicable Algebra in Engineering, Communication and Computing* 26.1 (2015), pp. 5–26. DOI: 10.1007/s00200-015-0251-x.
- [46] Eviatar Yemini, Albert Lin, Amin Nejatbakhsh, Erdem Varol, Ruoxi Sun, Gonzalo E. Mena, Aravinthan D.T. Samuel, Liam Paninski, Vivek Venkatchalam, and Oliver Hobert. “NeuroPAL: A Multicolor Atlas for Whole-Brain Neuronal Identification in *C. elegans*”. In: *Cell* 184.1 (2021), pp. 272–288. DOI: 10.1016/j.cell.2020.12.012.
- [47] Ruisong Zhou, Yuguo Yu, and Chunhe Li. “Revealing neural dynamical structure of *C. elegans* with deep learning”. In: *iScience* 27.5 (2024). DOI: <https://doi.org/10.1016/j.isci.2024.109759>.

IRVING INSTITUTE FOR CANCER DYNAMICS, DEPARTMENTS OF MATHEMATICS AND COMPUTER SCIENCE, COLUMBIA UNIVERSITY, NY

*Email address:* [andrew.blumberg@columbia.edu](mailto:andrew.blumberg@columbia.edu)

DATA SHAPE, CENTRE INRIA D’UNIVERSITÉ D’AZUR, BIOT, FRANCE

*Email address:* [mathieu.carriere@inria.fr](mailto:mathieu.carriere@inria.fr)

DEPARTMENT OF SYSTEMS BIOLOGY, COLUMBIA UNIVERSITY, NY

*Email address:* [jf3380@cumc.columbia.edu](mailto:jf3380@cumc.columbia.edu)

DEPARTMENT OF MATHEMATICS, INDIANA UNIVERSITY, IN

*Email address:* [mmandell@iu.edu](mailto:mmandell@iu.edu)